PHYSICAL REVIEW D **106,** 063017 (2022)

Exposing gravitational waves below the quantum sensing limit

Hang Yu[*]
TAPIR, Walter Burke Institute for Theoretical Physics, Mailcode 350-17,
California Institute of Technology, Pasadena, California 91125, USA

Denis Martynov
School of Physics and Astronomy and Institute of Gravitational Wave Astronomy,
University of Birmingham, Edgbaston, Birmingham B15 2TT, United Kingdom

Rana X. Adhikari
LIGO Laboratory, California Institute of Technology, MC 100-36, Pasadena, California 91125, USA

Yanbei Chen
TAPIR, Walter Burke Institute for Theoretical Physics, Mailcode 350-17,
California Institute of Technology, Pasadena, California 91125, USA

(Received 31 May 2022; accepted 6 September 2022; published 21 September 2022)

The sensitivities of ground-based gravitational-wave (GW) detectors are limited by quantum shot noise at a few hundred hertz and above. Nonetheless, one can use a quantum-correlation technique proposed by Martynov *et al.* [Phys. Rev. A **95**, 043831 (2017) to remove the expectation value of the shot noise, thereby exposing underlying classical signals in the cross spectrum formed by cross-correlating the two outputs in a GW interferometer's antisymmetric port. We explore here the prospects and analyze the sensitivity of using quantum correlation to detect astrophysical GW signals. Conceptually, this technique is similar to the correlation of two different GW detectors as it utilizes the fact that a GW signal will be correlated in the two outputs but the shot noise will be uncorrelated. Quantum correlation also has its unique advantages as it requires only a single interferometer to make a detection. Therefore, quantum correlation could increase the duty cycle, enhance the search efficiency, and enable the detection of highly polarized signals. In particular, we show that quantum correlation could be especially useful for detecting postmerger remnants of binary neutron stars with both short (< 1 s) and intermediate (~ 10–10^4 s) durations and setting upper limits on continuous emissions from unknown pulsars.

DOI: 10.1103/PhysRevD.106.063017

I. INTRODUCTION

To date, nearly 100 gravitational-wave (GW) events have been detected [1–5] by ground-based interferometers including Advanced Laser Interferometer Gravitational Wave Observatory (aLIGO [6]), Advanced Virgo [7], and KAGRA [8,9].

The most statistically powerful way to make a detection employs a technique known as matched filtering [10–13]. However, this technique has a potential limitation in that it requires accurate waveform templates. While this can be achieved for the inspiral stage of coalescing compact binaries, there are other potential GW sources whose theoretical waveforms might still have large theoretical uncertainties or be challenging to be constructed. This includes the postmerger signal of a binary neutron star (BNS) event (see, e.g., Ref. [14–16] and references therein). Other possibilities include the GW emission from core-collapsing supernovae [17–19], accretion disk instabilities [20], eccentric binary coalescence [21,22], etc. See also Ref. [17] and references therein.

Detection of these types of sources, therefore, calls for waveform-agnostic detection methods that do not assume a waveform template *a priori*. Multiple search algorithms for unmodeled GW signals have been developed following different principles, and examples of this family of algorithms include Coherent Wave Burst [23], Stochastic Transient Analysis Multidetector Pipeline [24], X-Pipeline [25], BayesWave [26,27], etc.

We present here a complementary method to the family of unmodeled burst search algorithms. This method utilizes a quantum-correlation technique [28]. In the current LIGO configuration, the optical signal produced by the main interferometer is split onto two photodetectors (PDs). Intuitively, a signal field produced by physical motions in the interferometer will be correlated among the two PDs,

---

[*] hangyu@caltech.edu

whereas the quantum shot noise will be uncorrelated. One can thus remove the quantum shot noise by cross-correlating the two PDs' outputs. This is in close analogy to how a GW signal could be detected by cross-correlating two different interferometers [24,29], except for that the correlation now requires only a single interferometer.

Quantum correlation has previously been used to constrain classical noise sources in LIGO [28,30]. In this work, we further explore the possibility of applying it to detect astrophysical GW events. As we will see later, quantum correlation can be especially beneficial for the search of signals associated with neutron stars (NSs) as they typically reside at high frequencies ($\gtrsim$100 Hz) where quantum shot noise limits a ground-based interferometer's sensitivity.

The rest of the paper is organized as follows. In Sec. II, we review the basics of quantum correlation and draw its connection with two-interferometer correlation to establish the signal-to-noise ratio for our subsequent analysis. This is followed by Sec. III, where we further discuss the potential benefits of quantum correlation. Then in Sec. IV we consider applying quantum correlation to detect astrophysical signals, including postmerger remnants of BNS events with short (< 1 s, Sec. IV A) and intermediate ($\sim$100 s, Sec. IV B) durations and continuous-wave emissions from Galactic pulsars (Sec. IV C). Finally, we conclude our study and discuss its limitations and future directions in Sec. V.

II. REMOVING QUANTUM SHOT NOISE

We begin our discussion by reviewing how one may remove the quantum shot noise in the readout spectrum using the cross-correlation technique described in [28]. We will assume first that there is no quantum squeezing injected into the interferometer, which represents the aLIGO configuration in the first and second observing runs. We will later discuss how one may extend this method to cope with squeezed light [31] (in particular, squeezed vacuum entering from the antisymmetric port of the interferometer [32]). In this work, we use the convention that we use E to denote an optical field and n the power response of PD. We choose the physical constants such that $[E^*E]$ has the unit of watts.

For aLIGO, the signal field leaving the interferometer's antisymmetric port is split onto two different PDs as shown in Fig. 1. In a semiclassical way, we can write the power fluctuation on each PD as

$$n_{1,2} = \mathrm{Re}[E_{\mathrm{lo}}^*(E_a \pm E_b + E_c)], \tag{1}$$

where the fields are defined as in Fig. 1. Specifically, E_{lo} is a local-oscillator field produced by an intentional detuning of the differential arm length (which is known as the "dc readout scheme" [33]). The field E_a corresponds to vacuum fluctuations entering the interferometer from the antisymmetric port and then returning to the readout PDs. Its interference with E_{lo} produces the quantum shot noise limiting a ground-based detector's high-frequency sensitivity. As we split the signal onto two different PDs, another vacuum field E_b enters from the open port of the beam splitter and it carries the same amount of fluctuation as the E_a field when there is no squeezing. Finally, the field E_c is produced by classical differential arm length changes. At frequency $\gtrsim$100 Hz, classical noises (e.g., coating thermal noise and gas phase noise) are expected to be small, and therefore $|E_c|$ is significant only when a high-frequency GW signal is present. The transfer function from a GW strain signal h at frequency f to the power fluctuation is given by the interferometer's optical response. It reads [28]

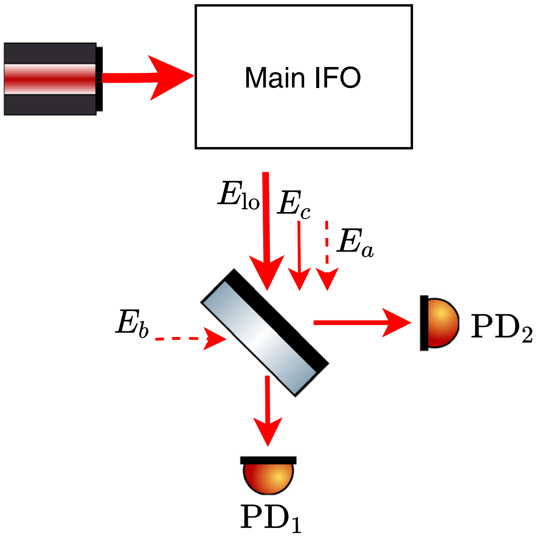

FIG. 1. Cartoon illustrating the readout port of an aLIGO-like GW detector. In the plot, "IFO" stands for the interferometer. The input laser marks its symmetric port and the signal is readout at the antisymmetric port.

$$\begin{aligned} Z(f) &\equiv 2|E_{\mathrm{lo}}|\frac{dE_c}{dL}(f)\frac{dL}{dh}(f), \\ &= |E_{\mathrm{lo}}|\frac{4\pi}{\lambda}(G_{\mathrm{a}}G_{\mathrm{p}}P_{\mathrm{in}})^{1/2}\frac{\tilde{t}_{\mathrm{i}}}{1-\tilde{r}_{\mathrm{i}}e^{-i4\pi fL/c}}\frac{dL}{dh}(f), \end{aligned} \tag{2}$$

where L, λ, and P_{in} are, respectively, the arm length, the laser wavelength, and the input power. The factor of 2 before E_c is because the GW signal is read out from the SUM channel, $n_{\mathrm{sum}} = n_1 + n_2$, corresponding to the sum of the two PDs' outputs. The factors G_{a} and G_{p} are the power buildup factors in the arm and power-recycling cavities, respectively. We further define

$$\tilde{r}_{\mathrm{i}} = \frac{r_{\mathrm{i}} - r_{\mathrm{s}}}{1 - r_{\mathrm{i}}r_{\mathrm{s}}} \quad \text{and} \quad \tilde{t}_{\mathrm{i}} = \frac{t_{\mathrm{i}}t_{\mathrm{s}}}{1 - r_{\mathrm{i}}r_{\mathrm{s}}}, \tag{3}$$

where t_{i} and t_{s} are the amplitude transmissivities of the input test mass and the signal-recycling mirror, and the reflectivities are given by $r_{\mathrm{i(s)}}^2 \simeq 1 - t_{\mathrm{i(s)}}^2$ when the optical losses are small. For aLIGO with an arm length of $L \simeq 4$ km, we further have $dL/dh \simeq L$ and $\exp(-i4\pi f L/c) \simeq 1 - i4\pi f L/c$. This leads to

$$Z(f) \simeq |E_{\mathrm{lo}}| \frac{4\pi}{\lambda} \frac{G_{\mathrm{arm}} G_{\mathrm{prc}}^{1/2} P_{\mathrm{in}}^{1/2}}{G_{\mathrm{src}}^{1/2}} \frac{f_-}{f_- + if} L, \tag{4}$$

where $f_- \simeq (1 - \tilde{r}_i)c/(4\pi L)$ is the coupled-cavity pole frequency and $G_{\mathrm{src}} \simeq (1 + r_s)^2/t_s^2$. Note that Eq. (4) reduces to the expression derived in Ref. [28]. For the future generation of GW detectors like the Cosmic Explorer (CE, [34–36]) with $L \simeq 40$ km, the approximation breaks down and therefore the full expression, Eq. (2), is used with the $dL/dh(f)$ term given by Ref. [37] (as done in noise budgeting codes like PYGWINC [38]).

If we denote the power spectral density (PSD) of $\mathrm{Re}[E_{\mathrm{lo}}^* E_{a,b}]$ as $P_{a,b}$ (whose expectation is $\langle P_a \rangle = \langle P_b \rangle = |E_{\mathrm{lo}}|^2 h\nu/2$ and units are $[\mathrm{W}^2\ \mathrm{Hz}^{-1}]$), then the PSD of the SUM channel due to the quantum shot noise (i.e., without E_c) is $P_{\mathrm{sum}} = 4P_a$, and the PSD of the shot noise in terms of the GW strain can be obtained by $\langle P_{\mathrm{sum}} \rangle / |Z(f)|^2$. Similarly, we can define a NULL channel as $n_{\mathrm{null}} = n_1 - n_2$ and its PSD is $P_{\mathrm{null}} = 4P_b$.

As shown in Ref. [28], we can get rid of the quantum shot noise through a quantum-correlation technique. Specifically, we compute the real part of the cross spectral density (CSD) of n_1 and n_2, which we denote as $C_{12} \equiv \mathrm{Re}[\mathrm{CSD}(n_1, n_2)]$, and its expectation is given by

$$\langle C_{12} \rangle = \langle P_a \rangle - \langle P_b \rangle + \langle P_c \rangle = \langle P_c \rangle. \tag{5}$$

We thus see the shot noise is removed in the CSD and we are left with only the classical length changes of the interferometer $\langle P_c \rangle$. On the other hand, we note the cancellation is done in the expectation. For a specific realization of C_{12} (i.e., a pixel in the spectrogram or the ft-map), the variance is given by

$$\sigma_{C_{12}}^2 = \frac{1}{2}(\langle P_a \rangle + \langle P_b \rangle)^2 = 2\langle P_a \rangle^2 = 2\langle P_b \rangle^2. \tag{6}$$

The signal-to-noise ratio (SNR) of each pixel is thus

$$\rho = \frac{C_{12}}{\sigma_{C_{12}}} \quad \text{and} \quad \langle \rho \rangle = \frac{\langle P_c \rangle}{\sqrt{2}\langle P_a \rangle} \propto \frac{h^2}{\langle P_a \rangle / |Z|^2}. \tag{7}$$

This is similar to how the SNR is defined in the case of two-interferometer correlation [24]. Note that the SNR is inversely proportional to the PSD of the shot noise $\langle P_a \rangle / |Z|^2$ (which has a unit of $[\mathrm{strain}^2/\mathrm{Hz}]$).

In fact, one can also remove the shot noise in expectation by computing the PSD of the NULL channel and then subtract it from the PSD of the SUM channel,

$$\langle P_{\mathrm{diff}} \rangle \equiv \langle P_{\mathrm{sum}} \rangle - \langle P_{\mathrm{null}} \rangle = 4(\langle P_a \rangle - \langle P_b \rangle + \langle P_c \rangle) = 4\langle P_c \rangle. \tag{8}$$

The variance on each pixel is

$$\sigma_{\mathrm{diff}}^2 = \sigma_{\mathrm{sum}}^2 + \sigma_{\mathrm{null}}^2 = 32\langle P_a \rangle^2. \tag{9}$$

We immediately see that the SNR obtained this way will be the same as the one obtained from the correlation technique.

How does the SNR of the quantum-correlation technique compare with the one obtained by cross-correlating two different interferometers (see, e.g., [24])? In the two-interferometer correlation scenario, we note that the signal's contribution to the CSD is $4P_c$ if we assume the two interferometers have identical configurations and signal responses. The standard deviation due to uncorrelated detector noise sources is $2\sqrt{2}\langle P_a \rangle$ in the CSD (assuming in the shot-noise limited regime). Therefore, the SNR is $\sqrt{2}P_c/\langle P_a \rangle$ for the two-interferometer correlation. On the other hand, if we perform quantum correlation on each interferometer individually first and then combine the SNR [Eq. (7)] in quadrature, the SNR is $P_c/\langle P_a \rangle$, which is $\sqrt{2}$ lower than directly correlating the two interferometers' outputs. The physical reason for this degradation is the following. As we utilize the E_b vacuum field to cancel out the expectation of the E_a field that causes the shot noise in the SUM channel, we inevitably introduce the fluctuations associated with E_b to the system as well. Therefore, the SNR is degraded and this is also the reason why a $\sqrt{2}$ appeared in the denominator of (7). Despite the loss in the SNR, the quantum-correlation technique nonetheless has a few unique advantages thanks to the fact that the signal field is produced by a single interferometer, which we will discuss in more detail in Sec. III. Therefore, it is still interesting to consider its application in detecting astrophysical signals in Sec. IV.

When E_a is squeezed and E_b is not, we see that the shot noise does not vanish in the CSD as shown in Eq. (5). Nonetheless, we can remedy the situation by also squeezing the E_b field such that we again have $\langle P_a \rangle = \langle P_b \rangle$. Note that this condition is needed only in the band where the shot noise dominates. Therefore, while the E_a field is anticipated to be squeezed in a frequency-dependent way (e.g., via a filter cavity [39,40]), a frequency-independent squeezing source is sufficient for the E_b field to achieve $\langle P_a \rangle = \langle P_b \rangle$ at $f \gtrsim$ a few × 100 Hz. Therefore, quantum correlation may be used not only for the archival LIGO data where the analysis above readily applies (as it has been used to constrain classical noise sources [28,30]), but also for future detectors like LIGO-A+ [41], LIGO-Voyager [42,43], LIGO-HF [44], the Neutron Star Extreme Matter Observatory [45], the Einstein Telescope [46–49], and CE [34–36] if an additional squeezed vacuum source would be installed for the E_b field so that $\langle P_a \rangle = \langle P_b \rangle$. We will assume this to be the case when applying quantum correlation for future detectors.

III. COMPARISON WITH TWO-INTERFEROMETER CORRELATION

Conceptually, we note quantum correlation is largely similar to the technique of cross-correlating two different interferometers [24]. They both utilize the fact that the signal is correlated among different readout channels, whereas the noise is uncorrelated. Compared to two-interferometer correlation, quantum correlation has the drawback that it only removes the quantum shot noise. And even in the shot-noise limited band, its sensitivity is slightly degraded due to the introduction of a new vacuum field into the system [which leads to the $\sqrt{2}$ factor in the denominator in Eq. (7)]. Nonetheless, quantum correlation has a few unique advantages thanks to the fact that *it requires only a single interferometer.*

First of all, a single detector naturally means a higher duty cycle compared to coincident observation between at least a pair of interferometers as required by the two-interferometer correlation. For instance, during the third observing run, each LIGO detector achieved a duty cycle of ≃75% individually, and the joint observation covered ≃60% of the time [30]. A higher duty cycle means that it is less likely for us to miss an astrophysical signal especially if the signal is transient in nature. Quantum correlation can thus be a critical backup plan for methods originally requiring two interferometers in the case that only one detector is online during a GW event.

Quantum correlation could also make searches for GW events more efficient, as to detect a signal from a single detector, one does not need to know the source's sky location.

To see this advantage, we first briefly review the basics to perform two-interferometer correlations [24,29]. Note that the GW strain observed by an interferometer I can be written as

$$h_I(t+\tau_I) = F_{I+}(\hat{\mathbf{\Omega}}, \psi)h_+(t) + F_{I\times}(\hat{\mathbf{\Omega}}, \psi)h_\times(t), \qquad (10)$$

where $h_{+(\times)}$ is the waveform in the $+(\times)$ polarization, $F_{I+(\times)}$ is the antenna response of interferometer I to each polarization, and it depends on the sky location of the source $\hat{\mathbf{\Omega}}$ and the polarization angle ψ. We further use t to denote the time when the GW wavefront arriving at a reference point and $\tau_I(\hat{\mathbf{\Omega}})$ the time for the wave to propagate from the reference to detector I. To perform two-interferometer correlation, one would need to account for the difference in a signal's arrival time and antenna responses in interferometers I and J, by applying a correction factor to align their outputs [24]

$$Q_{IJ} = \frac{2}{F_{I+}F_{J+} + F_{I\times}F_{J\times}} e^{2\pi i f \Delta\tau_{IJ}}, \qquad (11)$$

where $\Delta\tau_{IJ}$ is the time delay of the signal in different detectors. It can be further evaluated as $\Delta\tau_{IJ} = \hat{\mathbf{\Omega}} \cdot \mathbf{r}_{IJ}/c$, where $\mathbf{r}_{IJ}$ is the difference in position vectors of detectors I and J. For a source either with unknown location or poorly localized, we need to search over a large portion of the sky in order to perform cross-correlation between two interferometers. This could be a computationally expensive task.

For quantum correlation, this correction is not needed as the signal will reach the two readout PDs at effectively the same time (as $\Delta\tau_{II} = 0$) and the antenna response can be absorbed into an effective distance [11]. As a result, we would only need to search over the intrinsic source parameters, thereby reducing the computational cost. Note, however, that this does not mean we discard the information on the source's sky location. If we can detect the signal in two different interferometers, we can then readout the time delay between the interferometers as well as the difference in the SNR to infer the source's sky position. In other words, the sky location is inferred *after* the GW event's detection. Alternatively, we can also use quantum correlation as a first step to achieve the detection and to constrain the intrinsic source parameters, and then follow it up with more sensitive yet more computationally expensive analyses.

Yet another advantage of quantum correlation is that it works for polarized signals or if a signal contains high-order modes beyond just the 22 harmonic after decomposing into the spin-weighted spherical harmonics [50]. Imagine an extreme example. If interferometer I is sensitive only to the $+$ polarization and J only to the $\times$ polarization ($F_{I+} = F_{J\times} = 1$, $F_{I\times} = F_{J+} = 0$), then the cross-correlation between the two would not be able to detect a polarized signal with only the h_+ component. Nonetheless, with quantum correlation, we would at least be able to detect the signal in interferometer I.

Given these advantages, we investigate how quantum correlation may help us detect astrophysical GW signals in the following section.

IV. ASTROPHYSICAL APPLICATIONS

Quantum correlation enables removing the shot noise but not classical noise; it is mostly valuable for the detection of various GW signals related to NSs at shot-noise limited frequencies or $f \gtrsim 100$ Hz for ground-based GW observatories. In particular, quantum correlation could potentially help the detection of postmerger bursts of BNS events with short (< 1 s) or intermediate [$\sim\mathcal{O}(100)$ s] duration (Secs. IV A and IV B), as well as persistent or continuous GW emission from unknown pulsars (Sec. IV C).

As our focus is to detect the signal and extract the intrinsic parameters using a single detector, we will fix the source to have a face-on orientation and an antenna response $F_+ = 1, F_\times = 0$ for the cases in Secs. IV A and IV B. Changing the source's orientation, sky location, and polarization only affects the overall amplitude of the signal. Note, however, that these extrinsic parameters (such as the source's sky location) can be extract *after* the detection has been made in *multiple* detectors, though we deferred the analysis on extrinsic parameters to future studies.

A. Short-duration bursts

It has been postulated that if a BNS's total mass exceeds a maximum value allowed by a uniformly rotating star, its postmerger remnant could be a hypermassive NS that collapses in less than a second [14,51]. GW170817 [52], for example, is likely to have a total mass that can lead to a hypermassive NS [14,16,53].

The associated GW waveform of a hypermassive NS has been extensively studied by the literature (see, e.g., Refs. [54–61]). For the analysis here, we take GW waveforms provide in [55–57]. The comparison between the GW signal (the gray curve) and the shot-noise level of representative detectors (colored curves) are shown in the bottom-left panel in Fig. 2. We use cyan, olive, and purple to, respectively, represent aLIGO, Voyager, and CE and this convention will be used throughout this section. We place the merger at a distance of 100 Mpc and assume the SLy equation of state [62]. The waveform is filtered the same way as described in Ref. [56] to remove the premerger part.

To perform the quantum-correlation measurement, we convert the strain signal to power fluctuations on the PDs using Eq. (2) and superpose it with the other noise sources (dominated by the quantum shot noise in the band of interest). We then normalize each pixel by the standard deviation $\sigma_{C_{12}}$ [Eq. (6)]. A resultant normalized ft-map is presented in the top-right panel of Fig. 2. As a comparison, the corresponding ft-map for the SUM channel (i.e., the regular GW readout channel) is shown in the top-left panel. In this example, the merger happens at $t = 0.018$ s.

To detect the signal, we consider detection boxes with a size of (1/64 s, 192 Hz), corresponding to three pixels in the ft-map (see, e.g., the black box in the top-right panel of Fig. 2). The cumulative distribution of the total SNR in many realizations of signal-free boxes is further shown in the lower-middle panel of Fig. 2, serving as the background statistics for us to construct the detection threshold. Simulations here are performed over simulated Gaussian noises. Also shown in the vertical lines are the expected

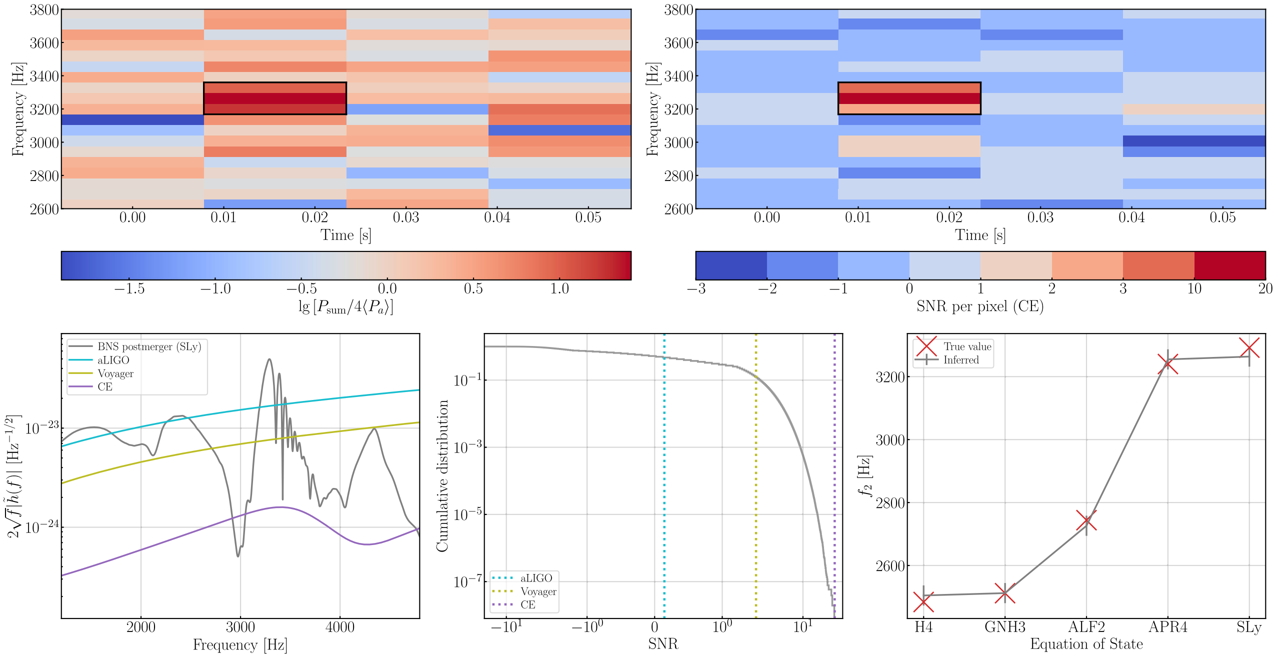

FIG. 2. Top left: example of an ft-map (spectrogram) of the SUM channel containing the postmerger signal (the premerger part is filtered out). The detector is assumed to have CE's sensitivity, and we have normalized each pixel by its signal-free expectation ($4\langle P_a\rangle$). Top right: the ft-map of the same data using quantum correlation. To detect the signal, we search over boxes spanning (1/64 s, 192 Hz) (i.e., three pixels), and the box leading to the highest total SNR is highlighted with a black boundary. Bottom left: comparison between the characteristic strain of a BNS postmerger signal (gray curve) and the sensitivity of representative GW detectors (colored curves). The source is placed at a distance of 100 Mpc with a face-on orientation and $F_+ = 1, F_\times = 0$. Bottom middle: cumulative distribution of background (signal-free) boxes with SNR greater than a value given by the x-axis. The vertical lines are the expected SNRs of the signal in the top-left panel in different detectors under the quantum-correlation technique. Bottom right: comparison between the inferred f_2 frequency (black pluses) and the true f_2 frequencies for different NS equations of state.

SNR inside the detection box of the signal shown in the bottom-left panel in various detectors.

Following Ref. [14], we define the root-sum-squared strain amplitude as

$$h_{\rm rss} = \sqrt{2\int (|\tilde{h}_+(f)|^2 + |\tilde{h}_\times(f)|^2) df}, \qquad (12)$$

where $\tilde{h}_{+(\times)}(f)$ are the Fourier transforms of $h_{+(\times)}(t)$. The efficiency of the algorithm is then analyzed in terms of the minimum $h_{\rm rss}$ required in order to make the false-alarm probability (FAP) lower than a certain threshold. Because our detection box is about 100 times shorter than the one used in Ref. [14], we thus choose a threshold of $\text{FAP} = 10^{-6}$ which is 100 times lower than the threshold used in Ref. [14]. This leads to $h_{\rm rss} = 1.5\times10^{-22}$, 3.8×10^{-23}, and 1.1×10^{-23} for the short-duration postmerger signal to be detected by aLIGO, Voyager, and CE, respectively. If we instead choose a more strict detection threshold of $\text{FAP} = 10^{-7}$, this only increases the value of $h_{\rm rss}$ by 6%–7%.

Besides detecting the signal itself, it is also of great significance to constrain the peak frequency of the postmerger signal. This is also known as the f_2 frequency following the convention used in Ref. [57] and it has been shown to contain critical information of the NS equation of state [63]. The f_2 peak frequency can be constrained from the ft-map by computing the SNR-weighted-mean frequency of the detection box that has the maximum SNR.

In the bottom-right panel of Fig. 2, we compare the inferred f_2 frequency (gray pluses) and the true f_2 frequency for a variety of NS equations of state, covering hard (H4 [64], GNH3 [65]), intermediate (ALF2 [66]), and soft (SLy [62], APR4 [67]) ones. In all the cases, we keep the source at 100 Mpc and assume CE's sensitivity in the detector. We find the fluctuation in the inferred value due to different noise realization is small < 10 Hz and the uncertainty in the inference is set by the resolution of the pixel. For all the equations of state we consider, the difference between the inferred value and the true one is less than half of the pixel's size, or 32 Hz, which we adopt as the size of the error bar when generating the gray markers in the plot. It is thus possible for us to use quantum correlation and future detectors to distinguish hard, intermediate, and soft equations of state.

B. Intermediate-duration bursts

For less massive BNS mergers, the remnant could be a supermassive NS whose mass is greater than the maximum value for a nonrotating NS. In this case, the GW signal could have a long duration, ranging from 10 to 10^4 s [68].

Following Refs. [14,15], here we consider the possibility that the merger produces a fast-spinning magnetar [69]. The subsequent spinning down of the magnetar follows a trajectory [70]

$$f(t) = f_0\left(1+\frac{t}{\tau}\right)^{1/(1-n)}, \qquad (13)$$

where f_0 is an initial GW frequency, τ is the spin-down timescale, and n is the braking index. The phase of the GW waveform is then given by

$$\Phi(t) = \Phi_0 + 2\pi\int_0^t f(t')dt', \qquad (14)$$

and the overall amplitude [70]

$$h_0(t) = \frac{4\pi^2 G}{c^4}\frac{\epsilon I}{d} f^2(t), \qquad (15)$$

where ϵ, I, and d are, respectively, the ellipticity, moment of inertia of the NS, and the distance to the source.

Consistent with Ref. [14], we adopt $(f_0, \tau, n) = (1000\ \text{Hz}, 100\ \text{s}, 5)$ to describe the spin-down trajectory. To set the amplitude, we further use $\epsilon = 0.01$, $I = 150\ M_\odot \text{km}^2 \simeq 3.0\times10^{38}\ \text{kg}\,\text{m}^2$, and $d = 40$ Mpc.

The signal (normalized by $\sigma_{C_{12}}$) is shown in the top-left panel of Fig. 3 and its superposition with detector noise (assuming CE's sensitivity) is shown in the top-right panel. Here the ft-map has a pixel size of $(1\ \text{s}, 1\ \text{Hz})$.

While the signal is too weak to be directly visible by eyes, it can nonetheless be detected if we search for excess power along certain trajectories including hundreds of pixels. Generic clustering and pattern-recognition algorithms (e.g., Refs. [71–74]) can be applied, yet as a proof-of-concept study, here we simply search over trajectories specified by Eq. (13) but with varying parameters. Each trajectory we search spans 500 pixels.

The resultant mean SNR along different trajectories is shown in the bottom-left panel of Fig. 3. When we hit the right parameters describing the signal, we note a sudden increase in the mean SNR along the trajectory. This allows us to simultaneously detect the signal and constrain its properties.

To quantitatively establish the sensitivity, we consider the cumulative distribution of the mean SNR along signal-free trajectories. The vertical lines represent the expected SNR of the signal (top-left panel of Fig. 3) in different detectors. If we choose a $\text{FAP} = 0.01$ as the detection threshold (which is consistent with Ref. [14]), this leads to $h_{\rm rss} = 9.6\times10^{-23}$, 2.5×10^{-23}, and 6.3×10^{-24} for aLIGO, Voyager, and CE, respectively.

C. Continuous-wave sources

Besides bursts, quantum correlation could potentially contribute to the search for GW emission from fast-rotating pulsars (see, e.g., [75–77]).

Suppose the total duration of observation is $T_{\rm obs}$. We divide the data into N nonoverlapping segments, and each segment has a duration of $T_{\rm FFT} = T_{\rm obs}/N$. We perform fast

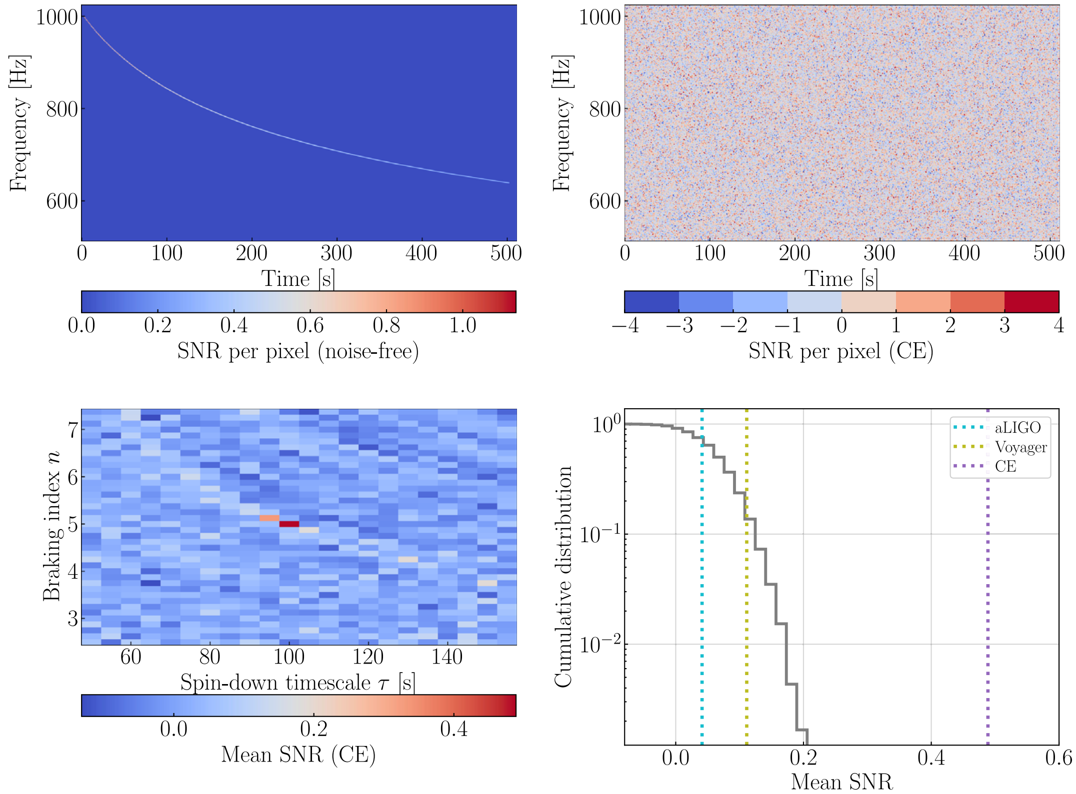

FIG. 3. Top left: ft-map of the spin-down signal of a magnetar without noise. Each pixel in the ft-map spans (1 s, 1 Hz). We place the magnetar at a distance of 40 Mpc and assume it has an ellipticity $\epsilon = 10^{-2}$. Top right: ft-map including both the signal and background noise (assuming CE sensitivity). Bottom left: mean SNR along trajectories specified by different spin-down timescale τ and braking index n [Eq. (13)]. When the parameters agree with the values describing the signal ($\tau = 100$ s; $n = 5$), we note a significant increase in the mean SNR, thereby allowing the signal to be detected and the intrinsic parameters to be constrained. Bottom right: cumulative distribution of background trajectories. The vertical lines are the expected SNRs of the signal in the top-left panel in different detectors under the quantum-correlation technique.

Fourier transfer (FFT) on each segment of data and compute the corresponding CSD for quantum correlation. The expected noise in the averaged CSD over N segments is approximated by the quadratic sum of the variance in the shot noise [Eq. (6)] and the nonvanishing classical noise $P_{c,\mathrm{cl}}$,

$$(C_{12}^2)_{\mathrm{noise}} \approx \sigma_{C_{12}}^2/N + P_{c,\mathrm{cl}}^2. \tag{16}$$

The resultant noise level is shown in the top panel in Fig. 4. We use dashed (dotted) lines to represent the estimated noise level after averaging over $N = 10^4$ ($N = 10^5$) segments. For aLIGO and Voyager, about 10^4 averages will be sufficient to reach the noise floor set by classical noise sources such as thermal noise [78] that cannot be removed by quantum correlation here. This corresponds to $T_{\mathrm{obs}} \simeq 4$ months if $T_{\mathrm{FFT}} = 1024$ s. For CE, the classical noise floor is significantly lower, and even with 10^5 averages ($T_{\mathrm{obs}} \simeq 3$ yr for $T_{\mathrm{FFT}} = 1024$ s), the sensitivity is still limited by the $\sigma_{C_{12}}^2/N$ term at 1000 Hz.

The noise level is to be compared with the expected signal strength in the CSD which we show in the solid lines for different values of ellipticities. The amplitude of the wave can still be computed from Eq. (15). We fix $I = 10^{38}$ kg m^2 and place the source at an averaged effective distance of $d = 10$ kpc. For a monochromatic GW emission with amplitude h at frequency f, we have

$$C_{12}(f) = \frac{1}{8} T_{\mathrm{FFT}} h^2(f). \tag{17}$$

Depending on the value of T_{FFT} (and hence the frequency resolution in the CSD), the Doppler effect due to the revolution of Earth around the Sun and the revolution of the pulsar itself if it is in a binary system can cause the signal to drift in multiple frequency bins. As a proof-of-concept study, we ignore here the complication due to the Doppler shift as it can be readily corrected for with existing algorithms such as FrequencyHough [79] (we would need to include the sky location of the source as search parameters here). Under this assumption, upper

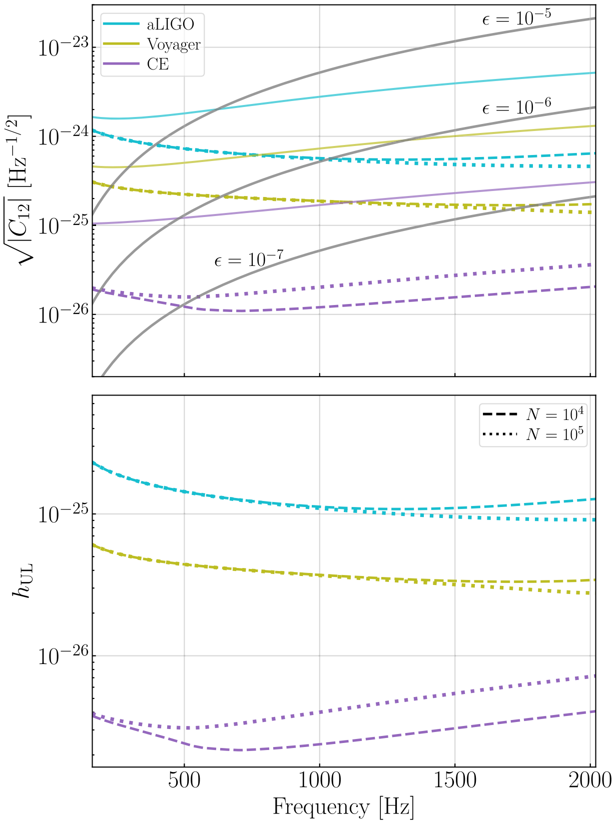

FIG. 4. Top: in the colored curves, we show the expected fluctuations in the CSD after averaging 10^4 (dashed) or 10^5 (dotted) segments of data, respectively corresponding to total observation time of 4 months and 3 years if each segment is 1024 s long. Different colors correspond to different detectors. As a comparison, the solid lines show the noise amplitude spectral density of each detector [note here we have divided each curve by 2 because the PSD due to signal E_c is $4\langle P_c\rangle$ in the SUM channel and $\langle P_c\rangle$ when doing quantum correlation; see Eq. (5)]. Also shown in the solid traces are expected signal strength $[\sqrt{\langle P_c/Z(f)\rangle}]$ due to pulsars whose GW frequencies correspond to the x-axis. We vary the value of ellipticity as labeled in the figure, while holding the pulsar's a distance at 10 kpc. Note here we have calibrated the CSD back to the strain unit. Bottom: upper limit on the strain h_{UL} based on the expected noise level [Eq. (18)]. The calculation assumes $T_{\mathrm{FFT}} = 1024$ s and a fiducial detection threshold of $\mathrm{SNR}_{\mathrm{th}} = 5$.

limits on the GW strain h_{UL} can then be obtained as [cf. Eq. (6) in Ref. [77]; see also Ref. [79]]

$$h_{\mathrm{UL}} = 2\sqrt{2\,\mathrm{SNR}_{\mathrm{th}}\frac{|(C_{12})_{\mathrm{noise}}|}{T_{\mathrm{FFT}}}}, \tag{18}$$

where $\mathrm{SNR}_{\mathrm{th}}$ is a threshold SNR to claim a detection (note our definition of SNR follows Ref. [24] and is defined in terms of power instead of amplitude as used in Ref. [79]). Depending on whether $|(C_{12})_{\mathrm{noise}}|$ is limited by $\sigma_{C_{12}}$ or $P_{c,\mathrm{cl}}$ [Eq. (16)], h_{UL} scales with T_{FFT} as $T_{\mathrm{FFT}}^{-1/4}$ or $T_{\mathrm{FFT}}^{-1/2}$ for given T_{obs}. In both cases, longer segment length is preferred. The upper limits are shown in the bottom panel of Fig. 4. Consistent with Ref. [77], we have assumed $T_{\mathrm{FFT}} = 1024$ s. We also adopted a fiducial detection threshold of $\mathrm{SNR}_{\mathrm{th}} = 5$.

Note that when applied to the detection of continuous GW emissions, quantum correlation provides a way to find hot pixels in the ft-map, which can then be fed to the FrequencyHough algorithm [79] as inputs. It thus complements the existing methods such as using the autoregressive estimation as proposed in Ref. [80]. While quantum correlation does not enhance the fundamental sensitivity, we could potentially benefit from its simplicity in removing the expectation value of the shot noise. Moreover, it naturally handles fluctuations and nonstationarities in the interferometer (as E_{lo} is a common reference field when computing $\langle P_a\rangle$ and $\langle P_b\rangle$; see the discussion in Sec. V). Though as a caveat, to reach the full sensitivity of quantum correlation, it requires the system to be well balanced. We will discuss this point more in Sec. V.

V. CONCLUSION AND DISCUSSION

In this work, we explored the possibility of detecting astrophysical GW events using quantum correlation, a technique that has been used by the LIGO instrumentation group to constrain classical noise in the LIGO interferometers [28,30]. We analyzed in a generic context the sensitivity of the technique in Sec. II. The main advantage of quantum correlation is that it requires only a single interferometer for the detection (Sec. III), which naturally leads to a higher duty cycle compared to two-interferometer correlation. Moreover, the signals captured by the two PDs in quantum correlation (Fig. 1) will share the same antenna response and arrival time, and consequently the detection search can be made more efficient as we do not need to search over extrinsic parameters like the sky location of the event to align the signals (at least for burst signals where the Doppler effect due to Earth's revolution and rotation can be ignored). This also allows us to detect highly polarized GW signals with quantum correlation. We then considered a few specific examples of using this technique to detect high-frequency GW signals in Sec. IV, including BNS postmerger remnants with both short (< 1 s; Sec. IV A) and intermediate (∼100 s; Sec. IV B) duration, as well as continuous GW emissions from pulsars (especially those at high GW frequencies; Sec. IV C).

Conceptually, the quantum-correlation technique can be understood in analogy to the correlation between two different interferometers (Sec. III). The quantum shot noise is uncorrelated among the two PDs reading out the GW signal (Fig. 1), thereby allowing its removal via cross-correlation. This allows us to adopt results developed for analyzing the cross-correlation between different interferometers. Indeed, our definition of the SNR for each pixel [Eq. (7)] follows closely Ref. [24], and multiple pattern-recognition algorithms [71,72] can be readily applied to search for the signal in the ft-map.

Meanwhile, Eq. (5) suggests that we can also view the quantum correlation as follows. By introducing the new field E_b, it provides us an estimation of $\langle P_a \rangle$ (as $\langle P_a \rangle = \langle P_b \rangle$), thereby allowing the removal of its expectation value in the (cross-)spectra. This further suggests that, if we know $\langle P_a \rangle$, we may also directly subtract it out and detect the GW signal as excess power in the residual spectra. In practice, to do the direct subtraction one would need to take into account the nonstationarity in the interferometer, which could mean extra complications compared to performing quantum correlation. For example, to directly predict the value of $\langle P_a \rangle$, one would need to know the instantaneous value of the local-oscillator field $E_{\rm lo}$, whereas the fluctuations in $E_{\rm lo}$ do not affect the quantum correlation because it serves as a common reference when computing $\langle P_a \rangle$ and $\langle P_b \rangle$. Nevertheless, doing the direct subtraction is an interesting direction to be explored by future studies as it might improve the sensitivity by avoiding the introduction of the uncertainties in P_b, which degrades the SNR in Eq. (5) by $\sqrt{2}$. To tackle the nonstationarities in the interferometer, one could utilize auxiliary channels in LIGO [81,82]. Furthermore, with auxiliary channels one could predict not only the expected spectrum of the quantum shot noise $\langle P_a \rangle$ but also other noise sources across the entire spectra. We plan to explore this possibility in follow-up studies.

We note that the quantum correlation may pick up instrumental glitches as hot pixels in the CSD. Nonetheless, there are at least two ways to distinguish between terrestrial glitches and astrophysical signals. One is to look for coincidence of hot pixels in multiple detectors. Indeed, this is how we can extract sky location of the source under the quantum-correlation technique. On the other hand, if we only find a signal candidate in a single detector, it may still have an astrophysical origin as its disappearance in the other detector(s) might be due to unfavorable antenna response. In this case, we can still veto instrumental glitches utilizing auxiliary channels as routinely done for the LIGO detector characterization [83–85].

For quantum correlation, uncertainties in the interferometer calibration [86,87] do not significantly affect the detection. This is because the signal is detected as excess power, which further means the phase of the signal is not used and the amplitude can be measured directly in terms of raw power in the readout PDs to establish the detection statistics. The calibration from power in the PDs to the astrophysical strain will affect mostly the subsequent inference of source parameters such as its distance and ellipticity yet less the detection of the signal itself.

We remind readers that our current analysis assumes the quantum enhancement is due to a squeezed vacuum (i.e., the E_a field in Fig. 1) injecting from the antisymmetric port of the interferometer. In this case, we can still perform quantum correlation by squeezing the E_b field with a similar amount (and the match is only needed in the high-frequency end in a frequency-independent way). Meanwhile, other techniques exists that could also enhance a detector's quantum noise level, see, e.g., reviews by Refs. [32,88]. The feasibility of quantum correlation with other quantum techniques thus is deferred to future studies.

As a proof-of-principle study, we have assumed the final beam splitter shown in Fig. 1 is an ideal 50-50 beam splitter, and when squeezed vacuum is used, we have assumed the squeezing level of the E_b field matches exactly the E_a field. In reality, imbalance exists inevitably, which can potentially degrade the performance of the quantum-correlation technique. One way to set the tolerance on the imbalance between the beam splitter's transmissivity and reflectivity and the mismatch of squeezing levels for different squeezers is by requiring [cf. Eq. (16)]

$$|\langle P_a \rangle - \langle P_b \rangle| \lesssim \max\left[P_{c,\rm cl}, \frac{\sigma_{C_{12}}}{\sqrt{N}}\right]. \tag{19}$$

For aLIGO, the requirement is set by the $P_{c,\rm cl}$ term, and satisfying the condition at 1000 Hz means the difference in $\langle P_a \rangle$ and $\langle P_b \rangle$ needs to be $\lesssim 3\%$. For CE, $P_{c,\rm cl}$ is significantly lower compared to the shot noise and the requirement is set by the number of averages N. In this case, the mismatch needs to be $\lesssim 0.4\%$ for $N = 10^5$. While failing to meet the requirement above will degrade the sensitivity to continuous-wave emission as discussed in Sec. IV C, it does not significantly hinder the sensitivity to burst signals (Secs. IV A and IV B). For detecting the burst signals, the requirement is set by

$$|\langle P_a \rangle - \langle P_b \rangle| \lesssim \sigma_{C_{12}}/\sqrt{N_{\rm pix}}, \tag{20}$$

where $N_{\rm pix}$ is the number of pixels along a detection trajectory. Since we typically have $N_{\rm pix} \lesssim 1000$ for burst signals, we have $(\sigma_{C_{12}}/\sqrt{N_{\rm pix}}) < \langle P_{c,\rm cl} \rangle$ especially for future detectors like CE. This leads to a more feasible requirement on the mismatch to be $\lesssim 4\%$. Indeed, the uncertainty in the squeezer's losses is estimated to be $\simeq 6\%$ during the third observing run [31]; see also [89]. Additionally, the E_a field will enter and then be reflected by the main interferometer and thus experience an additional loss. For the high-frequency end of interest, optomechanical effects can be ignored. The optical loss for E_a due to its reflection from the main interferometer is thus subdominant at a level $< 1\%$. Consequently, we are already close to the requirement and further improvement is expected with enhanced alignment control and mode matching.

ACKNOWLEDGMENTS

We thank the helpful comments and feedback from L. Sun, K. Riles, and other LVK colleagues. H. Y. is supported by the Sherman Fairchild Foundation. D. M. acknowledges the support of the Institute for Gravitational Wave Astronomy at the University of Birmingham, STFC (Grants No. ST/T006609/1, No. ST/S000305/1), and EPSRC research councils (Grants No. EP/V048872/1, No. EP/V008617/1). R. X. A is supported by NSF Grants No. PHY-1764464 and No. PHY-1912677. Y. C. is supported by the Simons Foundation (Grant Number 568762) and by NSF Grants No. PHY-2011961, No. PHY-2011968, and No. PHY–1836809.

[1] B. P. Abbott, R. Abbott, T. D. Abbott, S. Abraham, F. Acernese, K. Ackley, C. Adams, R. X. Adhikari, V. B. Adya, and C. Affeldt (LIGO Scientific Collaboration and Virgo Collaboration), GWTC-1: A Gravitational-Wave Transient Catalog of Compact Binary Mergers Observed by LIGO and Virgo during the First and Second Observing Runs, Phys. Rev. X **9**, 031040 (2019).

[2] R. Abbott *et al.* (LIGO Scientific Collaboration and Virgo Collaboration), GWTC-2: Compact Binary Coalescences Observed by LIGO and Virgo during the First Half of the Third Observing Run, Phys. Rev. X **11**, 021053 (2021).

[3] R. Abbott *et al.* (LIGO Scientific Collaboration, Virgo Collaboration, and KAGRA Collaboration), GWTC-3: Compact binary coalescences observed by LIGO and Virgo during the second part of the third observing run, arXiv: 2111.03606.

[4] T. Venumadhav, B. Zackay, J. Roulet, L. Dai, and M. Zaldarriaga, New binary black hole mergers in the second observing run of Advanced LIGO and Advanced Virgo, Phys. Rev. D **101**, 083030 (2020).

[5] S. Olsen, T. Venumadhav, J. Mushkin, J. Roulet, B. Zackay, and M. Zaldarriaga, New binary black hole mergers in the LIGO–Virgo O3a data, Phys. Rev. D **106**, 043009 (2022).

[6] J. Aasi *et al.* (LIGO Scientific Collaboration), Advanced LIGO, Classical Quantum Gravity **32**, 074001 (2015).

[7] F. Acernese *et al.* (VIRGO Collaboration), Advanced Virgo: A second-generation interferometric gravitational wave detector, Classical Quantum Gravity **32**, 024001 (2015).

[8] T. Akutsu *et al.* (KAGRA Collaboration), KAGRA: 2.5 generation interferometric gravitational wave detector, Nat. Astron. **3**, 35 (2019).

[9] T. Akutsu *et al.* (KAGRA Collaboration), Overview of KAGRA: Detector design and construction history, Prog. Theor. Exp. Phys. **2021**, 05A101 (2021).

[10] K. Cannon, A. Chapman, C. Hanna, D. Keppel, A. C. Searle, and A. J. Weinstein, Singular value decomposition applied to compact binary coalescence gravitational-wave signals, Phys. Rev. D **82**, 044025 (2010).

[11] B. Allen, W. G. Anderson, P. R. Brady, D. A. Brown, and J. D. E. Creighton, FINDCHIRP: An algorithm for detection of gravitational waves from inspiraling compact binaries, Phys. Rev. D **85**, 122006 (2012).

[12] C. Messick *et al.*, Analysis framework for the prompt discovery of compact binary mergers in gravitational-wave data, Phys. Rev. D **95**, 042001 (2017).

[13] T. Venumadhav, B. Zackay, J. Roulet, L. Dai, and M. Zaldarriaga, New search pipeline for compact binary mergers: Results for binary black holes in the first observing run of Advanced LIGO, Phys. Rev. D **100**, 023011 (2019).

[14] B. P. Abbott *et al.*, Search for post-merger gravitational waves from the remnant of the binary neutron star merger GW170817, Astrophys. J. **851**, L16 (2017).

[15] B. P. Abbott *et al.* (LIGO Scientific Collaboration, Virgo Collaboration), Search for gravitational waves from a long-lived remnant of the binary neutron star merger GW170817, Astrophys. J. **875**, 160 (2019).

[16] B. P. Abbott *et al.* (LIGO Scientific Collaboration, Virgo Collaboration), Properties of the Binary Neutron Star Merger GW170817, Phys. Rev. X **9**, 011001 (2019).

[17] R. Abbott *et al.* (LIGO Scientific Collaboration, VIRGO Collaboration, KAGRA Collaboration), All-sky search for long-duration gravitational-wave bursts in the third Advanced LIGO and Advanced Virgo run, Phys. Rev. D **104**, 102001 (2021).

[18] R. Abbott *et al.* (LIGO Scientific Collaboration, VIRGO Collaboration, KAGRA Collaboration), All-sky search for short gravitational-wave bursts in the third Advanced LIGO and Advanced Virgo run, Phys. Rev. D **104**, 122004 (2021).

[19] M. H. P. M. van Putten, A. Levinson, F. Frontera, C. Guidorzi, L. Amati, and M. Della Valle, Prospects for multi-messenger extended emission from core-collapse supernovae in the local Universe, Eur. Phys. J. Plus **134**, 537 (2019).

[20] M. H. van Putten, Proposed Source of Gravitational Radiation from a Torus around a Black Hole, Phys. Rev. Lett. **87**, 091101 (2001).

[21] E. A. Huerta, C. J. Moore, P. Kumar, D. George, A. J. K. Chua, R. Haas, E. Wessel, D. Johnson, D. Glennon, A. Rebei, A. M. Holgado, J. R. Gair, and H. P. Pfeiffer, Eccentric, nonspinning, inspiral, Gaussian-process merger approximant for the detection and characterization of eccentric binary black hole mergers, Phys. Rev. D **97**, 024031 (2018).

[22] B. P. Abbott *et al.* (LIGO Scientific, Virgo Collaborations), Search for eccentric binary black hole mergers with Advanced LIGO and Advanced Virgo during their first and second observing runs, Astrophys. J. **883**, 149 (2019).

[23] S. Klimenko, G. Vedovato, M. Drago, F. Salemi, V. Tiwari, G. A. Prodi, C. Lazzaro, K. Ackley, S. Tiwari, C. F. Da Silva, and G. Mitselmakher, Method for detection and reconstruction of gravitational wave transients with networks of advanced detectors, Phys. Rev. D **93**, 042004 (2016).

[24] E. Thrane, S. Kandhasamy, C. D. Ott, W. G. Anderson, N. L. Christensen, M. W. Coughlin, S. Dorsher, S. Giampanis, V. Mandic, A. Mytidis, T. Prestegard, P. Raffai, and B. Whiting, Long gravitational-wave transients and associated detection strategies for a network of terrestrial interferometers, Phys. Rev. D **83**, 083004 (2011).

[25] P. J. Sutton, G. Jones, S. Chatterji, P. Kalmus, I. Leonor, S. Poprocki, J. Rollins, A. Searle, L. Stein, M. Tinto, and M. Was, X-Pipeline: An analysis package for autonomous gravitational-wave burst searches, New J. Phys. **12**, 053034 (2010).

[26] N. J. Cornish and T. B. Littenberg, Bayeswave: Bayesian inference for gravitational wave bursts and instrument glitches, Classical Quantum Gravity **32**, 135012 (2015).

[27] N. J. Cornish, T. B. Littenberg, B. Bécsy, K. Chatziioannou, J. A. Clark, S. Ghonge, and M. Millhouse, BayesWave analysis pipeline in the era of gravitational wave observations, Phys. Rev. D **103**, 044006 (2021).

[28] D. V. Martynov, V. V. Frolov, S. Kandhasamy, K. Izumi, H. Miao, N. Mavalvala, E. D. Hall, R. Lanza *et al.*, Quantum correlation measurements in interferometric gravitational-wave detectors, Phys. Rev. A **95**, 043831 (2017).

[29] B. Allen and J. D. Romano, Detecting a stochastic background of gravitational radiation: Signal processing strategies and sensitivities, Phys. Rev. D **59**, 102001 (1999).

[30] A. Buikema, C. Cahillane, G. L. Mansell, C. D. Blair *et al.*, Sensitivity and performance of the advanced LIGO detectors in the third observing run, Phys. Rev. D **102**, 062003 (2020).

[31] M. Tse, H. Yu, N. Kijbunchoo, A. Fernandez-Galiana, P. Dupej, L. Barsotti, C. D. Blair, D. D. Brown *et al.*, Quantum-Enhanced Advanced LIGO Detectors in the Era of Gravitational-Wave Astronomy, Phys. Rev. Lett. **123**, 231107 (2019).

[32] T. Corbitt and N. Mavalvala, Quantum noise in gravitational wave interferometers: An overview and recent developments, Proc. SPIE Int. Soc. Opt. Eng. **5111**, 23 (2003).

[33] T. T. Fricke, N. D. Smith-Lefebvre, R. Abbott, R. Adhikari, K. L. Dooley, M. Evans, P. Fritschel, V. V. Frolov, K. Kawabe, J. S. Kissel, B. J. J. Slagmolen, and S. J. Waldman, DC readout experiment in Enhanced LIGO, Classical Quantum Gravity **29**, 065005 (2012).

[34] B. P. Abbott, R. Abbott, T. D. Abbott, M. R. Abernathy, K. Ackley, C. Adams, P. Addesso, R. X. Adhikari, V. B. Adya, C. Affeldt *et al.*, Exploring the sensitivity of next generation gravitational wave detectors, Classical Quantum Gravity **34**, 044001 (2017).

[35] D. Reitze *et al.*, Cosmic explorer: The U.S. contribution to gravitational-wave astronomy beyond LIGO, Bull. Am. Astron. Soc. **51**, 035 (2019), https://baas.aas.org/pub/2020n7i035/release/1.

[36] M. Evans, R. X. Adhikari, C. Afle, S. W. Ballmer, S. Biscoveanu, S. Borhanian, D. A. Brown, Y. Chen *et al.*, A horizon study for cosmic explorer: Science, observatories, and community, arXiv:2109.09882.

[37] R. Schilling, Angular and frequency response of LISA, Classical Quantum Gravity **14**, 1513 (1997).

[38] https://git.ligo.org/gwinc/pygwinc.

[39] L. McCuller, C. Whittle, D. Ganapathy, K. Komori, M. Tse, A. Fernandez-Galiana, L. Barsotti, P. Fritschel, M. MacInnis, F. Matichard, K. Mason, N. Mavalvala, R. Mittleman, H. Yu, M. E. Zucker, and M. Evans, Frequency-Dependent Squeezing for Advanced LIGO, Phys. Rev. Lett. **124**, 171102 (2020).

[40] Y. Zhao, N. Aritomi, E. Capocasa, M. Leonardi, M. Eisenmann, Y. Guo, E. Polini, A. Tomura *et al.*, Frequency-Dependent Squeezed Vacuum Source for Broadband Quantum Noise Reduction in Advanced Gravitational-Wave Detectors, Phys. Rev. Lett. **124**, 171101 (2020).

[41] B. P. Abbott *et al.* (KAGRA Collaboration, LIGO Scientific Collaboration, and VIRGO Collaboration), Prospects for observing and localizing gravitational-wave transients with Advanced LIGO, Advanced Virgo and KAGRA, Living Rev. Relativity **21**, 3 (2018).

[42] R. Adhikari, N. Smith, A. Brooks *et al.*, LIGO voyager upgrade concept (2017), LIGO Document T1400226.

[43] R. X. Adhikari, K. Arai, A. F. Brooks, C. Wipf *et al.*, A cryogenic silicon interferometer for gravitational-wave detection, Classical Quantum Gravity **37**, 165003 (2020).

[44] D. Martynov, H. Miao, H. Yang, F. H. Vivanco, E. Thrane, R. Smith, P. Lasky, W. E. East, R. Adhikari, A. Bauswein, A. Brooks, Y. Chen, T. Corbitt, A. Freise, H. Grote, Y. Levin, C. Zhao, and A. Vecchio, Exploring the sensitivity of gravitational wave detectors to neutron star physics, Phys. Rev. D **99**, 102004 (2019).

[45] K. Ackley, V. B. Adya, P. Agrawal, P. Altin, G. Ashton, M. Bailes, E. Baltinas, A. Barbuio *et al.*, Neutron star extreme matter observatory: A kilohertz-band gravitational-wave detector in the global network, Pub. Astron. Soc. Aust. **37**, e047 (2020).

[46] S. Hild, S. Chelkowski, A. Freise, J. Franc, N. Morgado, R. Flaminio, and R. DeSalvo, A xylophone configuration for a third-generation gravitational wave detector, Classical Quantum Gravity **27**, 015003 (2010).

[47] M. Punturo, M. Abernathy, F. Acernese, B. Allen, N. Andersson, K. Arun, F. Barone, B. Barr *et al.*, The third generation of gravitational wave observatories and their science reach, Classical Quantum Gravity **27**, 084007 (2010).

[48] S. Hild, M. Abernathy, F. Acernese, P. Amaro-Seoane, N. Andersson, K. Arun, F. Barone, B. Barr *et al.*, Sensitivity studies for third-generation gravitational wave observatories, Classical Quantum Gravity **28**, 094013 (2011).

[49] B. Sathyaprakash, M. Abernathy, F. Acernese, P. Ajith, B. Allen, P. Amaro-Seoane, N. Andersson, S. Aoudia, K. Arun, P. Astone *et al.*, Scientific objectives of Einstein telescope, Classical Quantum Gravity **29**, 124013 (2012).

[50] L. E. Kidder, Using full information when computing modes of post-Newtonian waveforms from inspiralling compact binaries in circular orbit, Phys. Rev. D **77**, 044016 (2008).

[51] T. W. Baumgarte, S. L. Shapiro, and M. Shibata, On the maximum mass of differentially rotating neutron stars, Astrophys. J. **528**, L29 (2000).

[52] B. P. Abbott *et al.* (LIGO Scientific Collaboration, Virgo Collaboration), GW170817: Observation of Gravitational

Waves from a Binary Neutron Star Inspiral, Phys. Rev. Lett. **119**, 161101 (2017).

[53] B. P. Abbott, R. Abbott, T. D. Abbott, F. Acernese, K. Ackley, C. Adams, T. Adams, P. Addesso *et al.*, Gravitational waves and gamma-rays from a binary neutron star merger: GW170817 and GRB 170817A, Astrophys. J. **848**, L13 (2017).

[54] K. Hotokezaka, K. Kiuchi, K. Kyutoku, T. Muranushi, Y.-i. Sekiguchi, M. Shibata, and K. Taniguchi, Remnant massive neutron stars of binary neutron star mergers: Evolution process and gravitational waveform, Phys. Rev. D **88**, 044026 (2013).

[55] K. Takami, L. Rezzolla, and L. Baiotti, Constraining the Equation of State of Neutron Stars from Binary Mergers, Phys. Rev. Lett. **113**, 091104 (2014).

[56] K. Takami, L. Rezzolla, and L. Baiotti, Spectral properties of the post-merger gravitational-wave signal from binary neutron stars, Phys. Rev. D **91**, 064001 (2015).

[57] L. Rezzolla and K. Takami, Gravitational-wave signal from binary neutron stars: A systematic analysis of the spectral properties, Phys. Rev. D **93**, 124051 (2016).

[58] T. Kawamura, B. Giacomazzo, W. Kastaun, R. Ciolfi, A. Endrizzi, L. Baiotti, and R. Perna, Binary neutron star mergers and short gamma-ray bursts: Effects of magnetic field orientation, equation of state, and mass ratio, Phys. Rev. D **94**, 064012 (2016).

[59] T. Dietrich, D. Radice, S. Bernuzzi, F. Zappa, A. Perego, B. Brügmann, S. Vivekanandji Chaurasia, R. Dudi, W. Tichy, and M. Ujevic, CoRe database of binary neutron star merger waveforms, Classical Quantum Gravity **35**, 24LT01 (2018).

[60] F. Zappa, S. Bernuzzi, D. Radice, A. Perego, and T. Dietrich, Gravitational-Wave Luminosity of Binary Neutron Stars Mergers, Phys. Rev. Lett. **120**, 111101 (2018).

[61] E. R. Most, A. Haber, S. P. Harris, Z. Zhang, M. G. Alford, and J. Noronha, Emergence of microphysical viscosity in binary neutron star post-merger dynamics, arXiv:2207.00442.

[62] F. Douchin and P. Haensel, A unified equation of state of dense matter and neutron star structure, Astron. Astrophys. **380**, 151 (2001).

[63] M. Shibata, Constraining Nuclear Equations of State Using Gravitational Waves from Hypermassive Neutron Stars, Phys. Rev. Lett. **94**, 201101 (2005).

[64] N. K. Glendenning and S. A. Moszkowski, Reconciliation of Neutron-Star Masses and Binding of the Lambda in Hypernuclei, Phys. Rev. Lett. **67**, 2414 (1991).

[65] N. K. Glendenning, Neutron stars are giant hypernuclei?, Astrophys. J. **293**, 470 (1985).

[66] M. Alford, M. Braby, M. Paris, and S. Reddy, Hybrid stars that masquerade as neutron stars, Astrophys. J. **629**, 969 (2005).

[67] A. Akmal, V. R. Pandharipande, and D. G. Ravenhall, Equation of state of nucleon matter and neutron star structure, Phys. Rev. C **58**, 1804 (1998).

[68] V. Ravi and P. D. Lasky, The birth of black holes: Neutron star collapse times, gamma-ray bursts and fast radio bursts, Mon. Not. R. Astron. Soc. **441**, 2433 (2014).

[69] C. Cutler, Gravitational waves from neutron stars with large toroidal B fields, Phys. Rev. D **66**, 084025 (2002).

[70] P. Lasky, N. Sarin, and L. Sammut, Long-duration waveform models for millisecond magnetars born in binary neutron star mergers (2017), LIGO Document T1700408.

[71] E. Thrane and M. Coughlin, Searching for gravitational-wave transients with a qualitative signal model: Seedless clustering strategies, Phys. Rev. D **88**, 083010 (2013).

[72] E. Thrane and M. Coughlin, Detecting Gravitation-Wave Transients at 5σ: A Hierarchical Approach, Phys. Rev. Lett. **115**, 181102 (2015).

[73] L. Sun and A. Melatos, Application of hidden Markov model tracking to the search for long-duration transient gravitational waves from the remnant of the binary neutron star merger GW170817, Phys. Rev. D **99**, 123003 (2019).

[74] S. Banagiri, L. Sun, M. W. Coughlin, and A. Melatos, Search strategies for long gravitational-wave transients: Hidden Markov model tracking and seedless clustering, Phys. Rev. D **100**, 024034 (2019).

[75] R. Abbott *et al.* (LIGO Scientific Collaboration, Virgo Collaboration), All-sky search in early O3 LIGO data for continuous gravitational-wave signals from unknown neutron stars in binary systems, Phys. Rev. D **103**, 064017 (2021).

[76] R. Abbott *et al.* (LIGO Scientific Collaboration, VIRGO Collaboration, KAGRA Collaboration), All-sky search for continuous gravitational waves from isolated neutron stars in the early O3 LIGO data, Phys. Rev. D **104**, 082004 (2021).

[77] R. Abbott *et al.* (LIGO Scientific Collaboration, Virgo Collaboration, KAGRA Collaboration), All-sky search for continuous gravitational waves from isolated neutron stars using Advanced LIGO and Advanced Virgo O3 data, arXiv:2201.00697.

[78] For simplicity, we consider here only the broadband classical noise and ignore sharp lines in the spectra.

[79] P. Astone, A. Colla, S. D'Antonio, S. Frasca, and C. Palomba, Method for all-sky searches of continuous gravitational wave signals using the frequency-Hough transform, Phys. Rev. D **90**, 042002 (2014).

[80] P. Astone, S. Frasca, and C. Palomba, The short FFT database and the peak map for the hierarchical search of periodic sources, Classical Quantum Gravity **22**, S1197 (2005).

[81] H. Yu, R. X. Adhikari, R. Magee, S. Sachdev, and Y. Chen, Early warning of coalescing neutron-star and neutron-star-black-hole binaries from the nonstationary noise background using neural networks, Phys. Rev. D **104**, 062004 (2021).

[82] H. Yu and R. X. Adhikari, Nonlinear noise cleaning in gravitational-wave detectors with convolutional neural networks, Front. Artif. Intell. **5**, 811563 (2022).

[83] R. Essick, L. Blackburn, and E. Katsavounidis, Optimizing vetoes for gravitational-wave transient searches, Classical Quantum Gravity **30**, 155010 (2013).

[84] R. Essick, P. Godwin, C. Hanna, L. Blackburn, and E. Katsavounidis, iDQ: Statistical inference of non-Gaussian noise with auxiliary degrees of freedom in gravitational-wave detectors, arXiv:2005.12761.

[85] D. Davis, M. Trevor, S. Mozzon, and L. K. Nuttall, Incorporating information from LIGO data quality streams into the PyCBC search for gravitational waves, arXiv:2204.03091.

[86] L. Sun *et al.*, Characterization of systematic error in Advanced LIGO calibration, Classical Quantum Gravity **37**, 225008 (2020).

[87] L. Sun *et al.*, Characterization of systematic error in Advanced LIGO calibration in the second half of O3, arXiv:2107.00129.

[88] S. L. Danilishin and F. Y. Khalili, Quantum measurement theory in gravitational-wave detectors, Living Rev. Relativity **15**, 5 (2012).

[89] J. Lough, E. Schreiber, F. Bergamin, H. Grote, M. Mehmet, H. Vahlbruch, C. Affeldt, M. Brinkmann, A. Bisht, V. Kringel, H. Lück, N. Mukund, S. Nadji, B. Sorazu, K. Strain, M. Weinert, and K. Danzmann, First Demonstration of 6 dB Quantum Noise Reduction in a Kilometer Scale Gravitational Wave Observatory, Phys. Rev. Lett. **126**, 041102 (2021).